

## A Modified Mazars Damage Model with Energy Regularization

M.R.T. Arruda<sup>a</sup>, J. Pacheco<sup>b</sup>, Luis M.S. Castro<sup>c</sup> and E. Julio<sup>d</sup>

<sup>a</sup> Research Associate, CERIS, Instituto Superior Técnico, Universidade de Lisboa, Portugal  
([mario.rui.arruda@tecnico.ulisboa.pt](mailto:mario.rui.arruda@tecnico.ulisboa.pt))

<sup>b</sup> Research Associate, CERIS, c5Lab, Linda-a-Velha, Portugal  
([jpacheco@c5lab.pt](mailto:jpacheco@c5lab.pt))

<sup>c</sup> Associate Professor, CERIS, Instituto Superior Técnico, Universidade de Lisboa, Portugal  
([luis.santos.castro@tecnico.ulisboa.pt](mailto:luis.santos.castro@tecnico.ulisboa.pt))

<sup>d</sup> Full Professor, CERIS, Instituto Superior Técnico, Universidade de Lisboa, Portugal  
([eduardo.julio@tecnico.ulisboa.pt](mailto:eduardo.julio@tecnico.ulisboa.pt))

**Abstract:** This paper presents a modified Mazars damage model, based on a strain formulation, for the physically nonlinear analysis of concrete structures. The main objective is to propose a modified damage model, in which both tension and compression damage evolution laws are regularized using a classical fracture energy methodology. The original loading functions are maintained, including their thermodynamic consistencies. The most relevant modification of the model is introduced in the damage evolutions laws, which are updated in order to produce similar stress-strain relations to those presented in *fib* Model Code 2010. The softening branch under both compressive and tensile strains is regularized with fracture energy. The damage model is then benchmarked with classical experimental and numerical tests considering monotonic loadings. The new constitutive relation was implemented in the commercial software ABAQUS via user subroutine UMAT. Research needs towards a definition of a generalized damage model with energy regularization are discussed and presented.

**Keywords:** Mesh Dependency, Fracture Energy, Mazars Damage Model, Finite Element Method, Concrete Softening Behaviour

### Nomenclature:

|            |                                    |
|------------|------------------------------------|
| $L_c$      | Characteristic length              |
| $d_c$      | Compressive damage                 |
| $\alpha_c$ | Compressive damage parameter       |
| $k$        | Compressive factor                 |
| $G_{fc}$   | Compressive fracture energy        |
| $A_c, B_c$ | Compressive softening parameters   |
| $f_{cm}$   | Compressive strength               |
| $g_{fc}$   | Compressive volume fracture energy |
| $f_{ctm}$  | Cracking stress                    |
| $k_r$      | Damage corrector                   |

|                    |  |
|--------------------|--|
| $d$                | Damage parameter                         |
| $\delta d$         | Damage variation                         |
| $E_d$              | Damaged elastic stiffness matrix         |
| $Y$                | Elastic energy release rate              |
| $E_0$              | Elastic stiffness matrix                 |
| $\tilde{\epsilon}$ | Equivalent strain                        |
| $\hat{\sigma}$     | Equivalent Stress                        |
| $\epsilon_{c1}$    | First compressive damage strain pointer  |
| $k_1$              | First compressive factor                 |
| $\epsilon_{d0}$    | Initial equivalent strain before damage  |
| $\sigma_{t0}$      | Initial tensile damage stress            |
| $\epsilon_{t0}$    | Initial tensile strain                   |
| $f$                | Loading function                         |
| $\sigma_{cmax}$    | Maximum compressive energy               |
| $\sigma_{tmax}$    | Maximum tensile stress                   |
| $\nu$              | Poisson coefficient                      |
| $\epsilon_{Ci}$    | Positive compressive parameter           |
| $\epsilon_i$       | Positive principal strains               |
| $\epsilon_{Ti}$    | Positive tensile parameter               |
| $E_{cm}$           | Secant elastic modulus                   |
| $\epsilon_{c2}$    | Second compressive damage strain pointer |
| $k_2$              | Second compressive factor                |
| $\Psi$             | Specific energy of Helmholtz             |
| $\epsilon$         | Strain                                   |
| $\sigma$           | Stress                                   |
| $d_T$              | Tensile damage                           |
| $\alpha_T$         | Tensile damage parameter                 |
| $\epsilon_{t1}$    | Tensile damage strain pointer            |
| $G_{ft}$           | Tensile fracture energy                  |

|                    |                                     |
|--------------------|-------------------------------------|
| $A_t, B_t$         | Tensile softening parameters        |
| $g_{ft}$           | Tensile volume fracture energy      |
| $\varepsilon_{cu}$ | Ultimate compressive strain pointer |
| $\varepsilon_{tu}$ | Ultimate tensile strain pointer     |

## 1 Introduction

### 1.1 Constitutive Relations for Concrete

Modelling concrete for general loading cases is still a challenging task. Numerous models have been proposed to simulate the mechanical behaviour of this material, but a consensus regarding the best strategy to adopt is still far from established. Before cracking, concrete is typically modelled as an isotropic continuum domain. This hypothesis usually leads to good results, notwithstanding concrete being a strongly heterogeneous composite material. After cracking, two approaches are commonly used to simulate the fracture-like phenomena that characterize its response [1-3]. The discrete cracking approach simulates the development of cracking through physical discontinuities introduced at the interfaces of elements, in which the amplitude and propagation of cracks are controlled by a given yield criteria [4-8]. Alternatively, the continuum approach treats materials as continuum domains and defines fracture as a damage accumulation process distributed in a finite zone on the continuum domain and physical discontinuities are not explicitly imposed [9-11]. This last approach is used in this work and is quite most common in commercial finite element software.

Most of the concrete models use internal material iterative procedures (e.g. using Euler integration scheme at a given finite element integration point). This iterative process is computational very heavy, and its non-convergence for large strain increments, may provide different structural responses, that are not expected for common structural designers. With the proposed modified Mazars damage model presented in this work, the number of inputs are quite small, there is no iterative integration scheme in the FE integration point, and well-known concrete constitutive relations for structural designers are used.

### 1.2 Objectives

The main objective of this work is to propose a modified Mazars damage model in which the thermodynamic consistency and loading functions are maintained as originally formulated. The core change is a fracture energy-based adjustment on the damage evolution laws. This adjustment regularizes the softening behaviour response and prevents mesh dependency. In order to promote the use of the Mazars damage model developed in the manuscript, the tension and compression damage behaviours of concrete are assumed as those presented in the softening laws of *fib* Model Code 2010 [12], since these are consensual for structural designers.

### 1.3 Research Significance

According to the authors' best knowledge, the Mazars damage model has been connected to the use of non-local damage regularization using Gauss weight functions and gradient models [13]. Even though these non-local regularizations are robust, they are not optimal when parallel processing is needed [14].

Some authors have used fracture energy with the Mazars damage model [15], but the constitutive relations based on stress vs strain are assemble using maximum element size, to avoid strong mesh dependency. In any case, this last method is not truly mesh independent since it relies on coarse meshes. In addition, it presents strong mesh sensibility in the presence of strong strain gradient fields or very distorted elements [16].

Contrary to non-local regularizations, fracture energy regularizations (the case of the model proposed in this paper), do not present any known problem when parallel processing is used. Another advantaged of using energy regularization, is that it is possible to use constitutive relationships that estimate fracture energy based on the compressive strength (e.g. those recommended in *fib* Model Code 2010) - this type of relationship is widely adopted and useful for non-linear structural design purposes [17], notwithstanding the uncertainty introduced by using constitutive models rather than experimental data (Sections 5.1 and 5.2 discuss this issue). In addition, the use of Mazars damage model, with compressive fracture regularization was never been published or discussed in the scientific community. Even the use of compressive energy regularization is commonly not use in other concrete damage models, and even most of them admit a certain level of mesh dependency, when compressive damage occurs. For this reason, the regularization of the Mazars damage model using fracture energy is proposed in this paper, in order to fill this gap in knowledge. The constitutive relation was implemented in the commercial software ABAQUS via user subroutine UMAT, using standard Fortran code.

## 2 Damage Model Formulation

Although the essential concept used damage mechanics was first introduced by Kachanov [18], the actual term “damage mechanics” was only quoted later in 1977 according to Krajcinovic [10]. Damage mechanics is an appealing formulation since it simulates fracture with relative simplicity, by simulating macro-cracks with stiffness degradation. The main difference from the concrete plasticity models, is that these do not include permanent strains in their original formulation. The loading functions that govern the expansion or contraction of damage depend mainly on the stress, strain and internal state variables. The concept of effective stresses is first presented in Rabotnov [19], and the damage variable physical meaning is developed, by affecting the initial material elastic stiffness with a proportional factor. The core concept of isotropic damage models is to accept a uniform degradation of the stiffness properties in all directions by assigning a stress-strain relation in terms of a damage scalar

Another approach to set up the theoretical basis of a new damage model, is to use thermodynamic laws [20, 21] and is based on the research reported in [22]. This approach is valuable for the scientific community, since it contributes to promote the robustness of new models, and theoretically validates them.

One of the most distinguished contributions to the improvement of concrete damage models was created by Lee and Fenves [23], and this formulation has been preferred by a several researchers [24]. This formulation has been implemented in the commercial software ABAQUS [25]. In the scientific community, successful non-linear analyses are executed using ABAQUS [26-28] and applied in particular structural design cases [29].

## 3 Regularization using Fracture Energy

The numerical solution for materials with strong stress softening depends on the FE mesh, and several studies found that coarse meshes produced better results than refined meshes [22]. When damage is developed and softening occurs, the governing differential equations lose ellipticity and the boundary value problem describing the structural response becomes ill-posed [30], being the strain distribution

localized in a thin band, with the width depending on the element size. The total volume of dissipated energy vanishes, due to the length of thin band length trending to zero, as the mesh is refined. To preserve the objectivity of the mesh and to recover the well-posedness of the boundary value problem, several regularization methods are recommended in [31].

A simple and efficient regularization technique is based on the use of fracture energy, which is associated with the total energy released to propagate the crack. This regularization is implemented by correcting the post-peak slope of the stress vs strain diagram as a function of the element size.

When using fracture energy regularization, higher/smaller elements will be associated with smaller/larger computational values of volume fracture energy, therefore, removing the consequence of energy dissipation volume.

When this type of regularization is used, the energy dissipated in a band of cracking elements does not depend on their width [32], but material behaviour remains dependent on the adopted discretization, meaning damage localization still occurs. In any case, the force vs displacement structural response is regularized, and it isn't mesh dependent.

## 4 Mazars Concrete Damage Model

In this section the constitutive relation for the concrete damage models proposed by Mazars [33] is discussed. Its hypothesis is founded on the base of an elastic damage isotropic behaviour. This model assumes the following premises: i) damage evolves/occurs only due to positive strains in the principal directions, which indirectly promotes “smeared crack grow”; ii) only one scalar damage variable  $d$  is defined, this is due to the damage model being isotropic; iii)  $d = 1$  represents the material as totally damaged, and it is limited in the interval  $0 \leq d \leq 1$ ; iv) no permanent strains are admitted, and the unloading path is linear, therefore, no hysteretic loops.

Even though the premises adopted by the Mazars damage model may seem modest/simple, they are also used popular open FE software [34] for static and dynamic analysis. This is due to the cycle structural behaviour of RC structures being mainly governed by the plastic strains and hysteretic loops of the steel rebars. In any case for simple plain concrete structures, under monotonic static load, the Mazars damage model is adequate.

### 4.1 Thermodynamic Framework

The specific energy of Helmholtz,  $\Psi$ , is given by equation (1), in the Mazars concrete damage model. The internal state variable is the damage parameter  $d$ , and the primary state variable is the strain tensor,  $\varepsilon$ . The elastic energy release rate and the stress tensor,  $Y$  and  $\sigma$ , are the associated variables defined by equation (2). Due to  $\det(E_0) \geq 0$ , the associated variable  $Y$  is always positive, therefore, the 2<sup>nd</sup> principal of thermodynamic is respected, as depicted in equation (3) as long as the Kuhn-Tucker condition [22] is fulfilled. To satisfy all these conditions in the Mazars model, it is only required that the increment of damage is always positive or null (damage state variables never decrease), as indicated by equation (4).

$$\Psi(\varepsilon, d) = \frac{1}{2}(1 - d)\{\varepsilon\}^t[E_0]\{\varepsilon\} \quad (1)$$

$$\begin{cases} \{\sigma\} = \frac{\partial \Psi}{\partial \{\varepsilon\}} = (1 - d)[E_0]\{\varepsilon\} \\ Y = -\frac{\partial \Psi}{\partial d} = \frac{1}{2}\{\varepsilon\}^t[E_0]\{\varepsilon\} \end{cases} \quad (2)$$

$$-\left(\frac{\partial \Psi}{\partial d}\right) \delta d \geq 0 \quad (3)$$

$$\delta d \geq 0 \quad (4)$$

To assemble a concrete damage model, it is required to describe a loading function that may be governed by the state variables, as expressed in (10). The goal of this function is to confirm if the damage evolution fulfils with the loading-unloading (Kuhn-Tucker) conditions depicted in equation (5).

$$f \leq 0 \quad \text{and} \quad \delta d \geq 0 \quad \text{and} \quad \delta d \cdot f = 0 \quad (5)$$

## 4.2 Model Formulation

Mazars defined [33], the constitutive relation for non-linear concrete behaviour using the classical equation (6), where  $E_d$  is the local damaged stiffness matrix at a given time step. Matrix  $E_d$  may be calculated using the description in equation (7), where  $E_0$  is the local stiffness matrix for the undamaged material. This matrix  $E_0$  has constant values since undamaged material behaviour is assumed as isotropic linear elastic.

$$\{\sigma\} = [E_d]\{\varepsilon\} \quad (6)$$

$$[E_d] = (1 - d)[E_0] \quad (7)$$

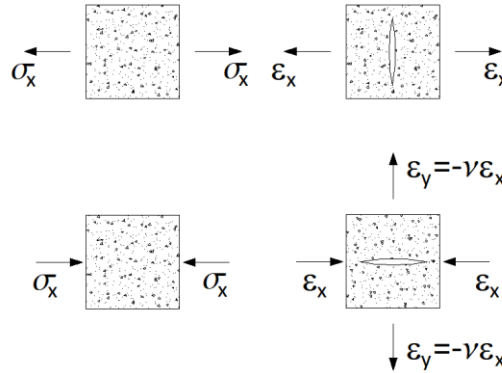


Figure 1 – Damage behaviour in Mazars model, for tensile and compressive behaviour.

The positive principal strains,  $\varepsilon_i$ , governs the damage evolution for both tensile or compressive behaviour, as illustrated in Figure 1. In this framework, Mazars defines the equivalent strain,  $\tilde{\varepsilon}$ , calculated according to equation (8),

$$\tilde{\varepsilon} = \sqrt{\langle \varepsilon_1 \rangle_+^2 + \langle \varepsilon_2 \rangle_+^2 + \langle \varepsilon_3 \rangle_+^2} \quad (8)$$

with

$$\langle a \rangle^\pm = \frac{1}{2}(a \pm |a|) \quad (9)$$

The loading function,  $f$ , depends on the scalar variable equivalent strain,  $\tilde{\epsilon}$ , and on a scalar parameter,  $\epsilon_{d0}(d)$ , which delimits the evolution of the elastic domain. Initially the value of  $\epsilon_{d0}$  is a material constant, but after the initiation of damage the value of  $\epsilon_{d0}$  is updated to  $\epsilon_{d0}(d) = \tilde{\epsilon}$ .

$$f(\tilde{\epsilon}, \epsilon_{d0}) = \tilde{\epsilon} - \epsilon_{d0}(d) = 0 \quad (10)$$

In materials terms,  $\epsilon_{d0}(d)$  is a scalar measure of the largest equivalent strain level achieved in the load history of the concrete. If  $f < 0$ , unloading occurs and no modification in the damage variable is detected. Else, a rise of the damage variable follows and the new value for  $d$  is acquired as a linear combination of two scalar and independent variables  $d_T$  and  $d_C$  (11):

$$d = \alpha_T d_T + \alpha_C d_C \quad (11)$$

### 4.3 Original Damage Evolution

In its original work, Mazars [33] suggested a simple expression to calculate  $d_T$  and  $d_C$ , to remove any iterative process required at the material level (contrary to classical plasticity). To obtain this, the damage evolutions, is given separately for both tensile and compressive behaviour (12).

$$\begin{aligned} d_t &= 1 - \frac{\epsilon_{d0}(1 - A_t)}{\tilde{\epsilon}} - \frac{A_t}{e^{B_t(\tilde{\epsilon} - \epsilon_{d0})}} \\ d_c &= 1 - \frac{\epsilon_{d0}(1 - A_c)}{\tilde{\epsilon}} - \frac{A_c}{e^{B_c(\tilde{\epsilon} - \epsilon_{d0})}} \end{aligned} \quad (12)$$

The softening behavior of stress vs strain diagram, is controlled by the coefficients  $A_T$ ,  $A_C$ ,  $B_T$ ,  $B_C$ , which are the concrete material parameters. Classical uniaxial experimental setups with controlled displacement, can be used to identified these parameters. For the triaxial case, the values of  $\alpha_T$  and  $\alpha_C$  are acquired considering adjusted strain vectors for tension and compression, as depicted by:

$$\begin{aligned} \epsilon_{Ti} &= \frac{1 + \nu}{E} \langle \hat{\sigma}_i \rangle_+ - \frac{\nu}{E} \sum_k \langle \hat{\sigma}_k \rangle_+ \\ \epsilon_{Ci} &= \frac{1 + \nu}{E} \langle \hat{\sigma}_i \rangle_- - \frac{\nu}{E} \sum_k \langle \hat{\sigma}_k \rangle_- \end{aligned} \quad (13)$$

These vectors are calculated using the principal positive effective stresses, calculated in accordance with (14) and (15).

$$\{\hat{\sigma}\} = [E_0]\{\epsilon\} \quad (14)$$

$$\langle \{\hat{\sigma}\} \rangle_{\pm} = \frac{1}{2} (\{\hat{\sigma}\} \pm |\{\hat{\sigma}\}|) \quad (15)$$

The calculation of coefficients  $d_T$  and  $d_C$  may be performed using equation (16) with only positive components of the vectors  $\epsilon_T$  and  $\epsilon_C$ . This is due to the first hypothesis of the Mazars model that only

positive strains produce damage. To promote stabilization during the convergence process, it is considered that these values remain constant during a given time step.

$$\begin{aligned} \varepsilon_V^+ &= \sum_i \langle \varepsilon_{Ti} \rangle_+ + \sum_i \langle \varepsilon_{Ci} \rangle_+ \\ \alpha_T &= \frac{\sum_i \langle \varepsilon_{Ti} \rangle_+}{\varepsilon_V^+} ; \quad \alpha_C = \frac{\sum_i \langle \varepsilon_{Ci} \rangle_+}{\varepsilon_V^+} \end{aligned} \quad (16)$$

For particular uniaxial case, the concrete is subjected to either tensile or compressive behaviour, so coefficients  $\alpha_T$  and  $\alpha_C$  can only adopt values 1 or 0. The expressions (8) and (16) are simplified resulting in the new coefficients given by (17) and the respective equivalent strains (18).

$$\begin{cases} \alpha_T = 1; \alpha_C = 0 & \text{if } \varepsilon \geq 0 \\ \alpha_T = 0; \alpha_C = 1 & \text{if } \varepsilon < 0 \end{cases} \quad (17)$$

$$\tilde{\varepsilon} = \begin{cases} \varepsilon & \text{if } \varepsilon \geq 0 \\ -\nu\sqrt{2}\varepsilon & \text{if } \varepsilon < 0 \end{cases} \quad (18)$$

#### 4.4 Proposed Modification

In most of the academic implementations, the Mazars damage model is combined with the use of a regularization technique considering non-local integral [35] or gradient [13] models. These regularization techniques are very effective in ensuring objectivity of the numerical solutions, but they are not disseminated in the industry and are not common in commercial FE software. This is due to the known difficulties in performing efficient parallel computation with legacy solvers [36], whenever non-local regularization is implemented. Moreover, the use of integral non-local and gradient models may lead to quite heavy computational procedures.

Fracture energy regularization provides a less robust method when compared with the other two regularization techniques referred before. Nonetheless this type of regularization is widely adopted by the industry, guides of the *fib* [17] and commercial FE software, without presenting any major drawbacks when parallel processing algorithms are to be adopted [37].

For this reason, this work recommends the use of fracture energy regularization for the Mazars damage model, by proposing new damage evolution laws for tension and compression behaviour. The original formulation of Mazars, including all thermodynamic consistencies referred previously are kept unchanged. To preserve the essence of the original Mazars loading function, all of the damage evolution laws are rewritten in terms of the equivalent strain parameter, as defined by equation (8).

##### 4.4.1 Tension Damage Behaviour

For tension behaviour, a classical exponential law for softening is proposed. The initial non-linear behaviour follows the relationship presented in MC2010 [12] - see Figure 2. The initial stress-strain behaviour is linear (branch OA) and is followed by non-linear behaviour with damage (branch AB). Afterwards, an exponential softening law is used to model the progression of damage (branch BC). This model accurately reproduces the material behaviour typically observed in uniaxial tensile strength tests [35, 38]. The tension damage evolution law is defined by:



$$d_T = 1 - \frac{\varepsilon_{d0}}{k_r \xi} \exp\left(\frac{\varepsilon_{t1} - \xi}{\varepsilon_{tu} - \varepsilon_{t1}}\right) \quad (19)$$

All parameters and physical quantities present in equation (19) are defined by:

$$\sigma_{t0} = k_r f_{ctm} ; \sigma_{tmax} = f_{ctm} ; \varepsilon_{t0} = \varepsilon_{d0} ; k_r = 0.9 \quad (20)$$

$$\varepsilon_{t1} = \max\{0.015\%; 1.1\varepsilon_{d0}\} ; \varepsilon_{tu} = \frac{G_{ft}}{L_c f_{ctm}} + \varepsilon_{t1} ; g_{ft} = \frac{G_{ft}}{L_c} \quad (21)$$

Some of the variables are described in MC2010, while others are redefined:  $f_{ctm}$  is the mean uniaxial tensile stress of concrete;  $\varepsilon_{tu}$  corresponds to the equivalent ultimate strain for bilinear softening and, as shown in Figure 2, may be computed using the tangent to the exponential softening law computed at point B;  $\varepsilon_{t1}$  is a fixed value provided by MC2010;  $L_c$  is the characteristic length of the element;  $G_{ft}$  and  $g_{ft}$  are the fracture energy and volume fracture energy of the material respectively. The area defined by triangle B- $\varepsilon_{tu}$ - $\varepsilon_{t1}$  corresponds to half of the volume fracture energy, while the other half corresponds to the area defined between the exponential softening curve and the tangent to the exponential softening curve computed at point B.

MC2010 defines softening under uniaxial tension using a bilinear law. This may lead to convergence problems when damage approaches the value 1.0. This is not the case when the exponential softening law is used, ensuring a stable numerical behaviour for the constitutive model.

It is important to point out that the consideration of branch AB is somehow irrelevant in terms of structural response, due to the fast cracking of concrete at the initial stages of the structural response. For all numerical examples presented in Section 7 of this paper, except for the last, a simplification is considered: the path OAB of Figure 3 is simplified to branch OB (that is,  $\varepsilon_{t1} = \varepsilon_{d0}$  is assumed). This option improves computational efficiency and has virtually no effect on the output of the numerical modelling.

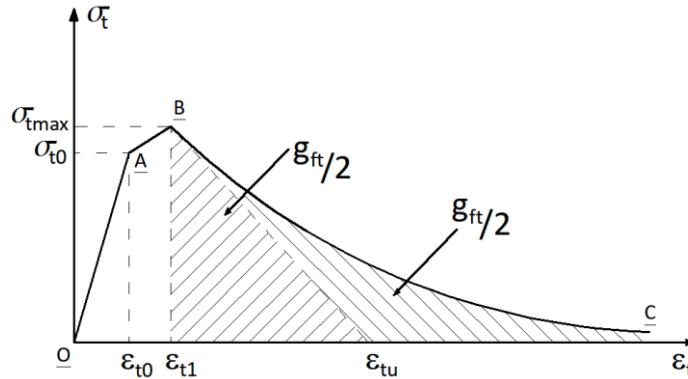


Figure 2 – Tension vs equivalent strain for the modified Mazars damage model.

#### 4.4.2 Compression Damage Behaviour

The modelling of compression behaviour is an adaptation of the MC2010 stress-strain relation for uniaxial compression. The MC2010 relation is used until the onset of softening (path OAB of Figure 3). Even if no consensus exists when defining an adequate softening branch (path BCDE) [39], the simplification introduced in [17] is adopted here. To ensure simplification and to promote computational efficiency, a simple bilinear function is adopted: stress is constant in branch BC and decreases linearly in branch CD (Figure 3).

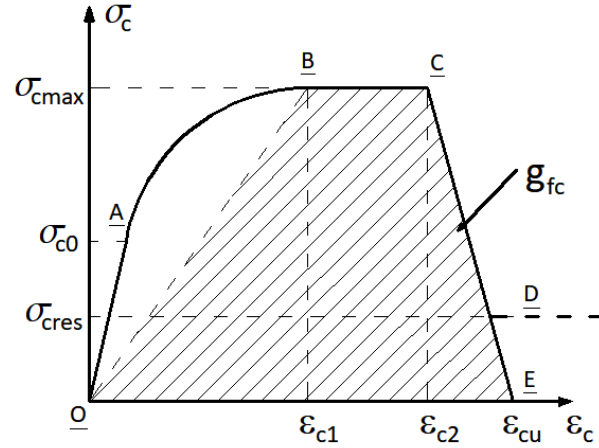


Figure 3 – Compression vs equivalent compression strain for the modified Mazars damage model.

To minimize convergence problems, and as suggested in *fib* bulletin 45 [17], the model adopted here admits a residual compressive stress. Damage initiates at point A and may increase throughout all loading history. To measure the volume fracture energy ( $g_{fc}$ ), the assumption introduced in [40] is adopted. Under this condition, and neglecting the residual stress, the equivalent ultimate compressive strain is extrapolated, as indicated in equation (22).

$$g_{fc} = \frac{G_{fc}}{L_c} = \sigma_{cmax} \times \left( \frac{\varepsilon_{cu} + (\varepsilon_{c2} - \varepsilon_{c1})}{2} \right) \quad (22)$$

The compressive damage evolution law is defined by:

$$d_c = \begin{cases} 1 - \frac{(k \times \bar{\varepsilon}_c - \bar{\varepsilon}_c^2) f_{cm}}{(1 + (k - 2) \times \bar{\varepsilon}_c) E_{cm} \bar{\varepsilon}_c} & \text{if } \check{\varepsilon}_c \leq \varepsilon_{c1} \\ 1 - \frac{f_{cm}}{E_{cm} \check{\varepsilon}_c} & \text{if } \varepsilon_{c1} < \check{\varepsilon}_c \leq \varepsilon_{c2} \\ 1 + \frac{k_1}{E_{cm}} - \frac{k_2}{E_{cm} \check{\varepsilon}_c} & \text{if } \varepsilon_{c2} < \check{\varepsilon}_c \leq \varepsilon_{cu} \end{cases} \quad (23)$$

where

$$\sigma_{cmax} = f_{cm}; \quad \check{\varepsilon}_c = \frac{\bar{\varepsilon}_c}{\nu\sqrt{2}}; \quad \bar{\varepsilon}_c = \frac{\check{\varepsilon}_c}{\varepsilon_{c1}}; \quad k = \frac{1.05 E_{cm} \varepsilon_{c1}}{f_{cm}}; \quad k_1 = \frac{f_{cm}}{(\varepsilon_{cu} - \varepsilon_{c2})}; \quad k_2 = f_{cm} + k_1 \times \varepsilon_{c2} \quad (24)$$

Even if some modifications required by the use of Mazars damage models combined with the fracture energy regularization were introduced, the compressive damage evolution law (23) and the adopted variables (24) agree with the stress-strain constitutive relation for uniaxial compression presented in MC2010. In these equations,  $f_{cm}$  is the mean compressive strength of concrete;  $E_{cm}$  is the secant Young's modulus;  $\varepsilon_{c1}$  and  $\varepsilon_{c2}$  are strain parameters adopted from MC2010;  $k$ ,  $k_1$  and  $k_2$  correspond to parameters that describe the constitutive curve;  $\bar{\varepsilon}_c$  is a unidimensional strain ratio provided in MC2010;  $G_{fc}$  and  $g_{fc}$  are the compressive fracture energy and the volume compressive fracture energy defined for the material, respectively.

## 5 Specimen Test

In this section, the tensile and compressive curves of the proposed modified Mazars model are used to model the behaviour of representative volume specimens. The results obtained with the proposed model are then compared to previous stress vs strain curves presented by other authors, and to the MC2010 curves. This is important since it is necessary to validate the new modified Mazars model for future design purposes. For both tests concrete of the C25/30 strength class is used.

The definition of the “representative volume specimen” depends on the type of material being considered [22, 30, 41, 42]. For the case of concrete, cylindrical specimens are usually recommended, but their length is still an open issue when one wants to define both tension and compression fracture energies [43, 44]. To solve this problem, the authors used the relevant information obtained in previous experimental campaigns aiming to determine compressive fracture energy [45, 46], in which specimens with a height  $\geq 300\text{mm}$  led to constant stable energy fracture results. This value agrees with the minimum characteristic length provided by [47], which served as a guideline to Model Code 1990 [48]. Therefore, a specimen with a height equal to 300 mm is used and  $L_c = 250\text{mm}$  is assumed to take into account the Saint-Venant effect in the upper and lower load part of the cylinder caused by Poisson effects and friction between the specimen and the test plates.

### 5.1 Tensile Behaviour

Figure 4 shows the tensile stress vs tensile strain diagram obtained with the proposed modified Mazars damage model. The original Hillerborg [49] and the MC2010 [12] with tension stiffening relationships are also plotted. In order to directly compare the curves of the two models, it is admitted that  $\varepsilon_{t0} = \varepsilon_{t1}$ . The tensile fracture energy was estimated using the relationship proposed in MC2010 [12] and defined by equation (25). In general, this value is approximately double the one provided by Hilsdorf for normal concrete, which is the basis of MC1990 [47] and is defined by equation (26).

$$G_{ft} = 73 \times (f_{cm})^{0.18} \quad (25)$$

$$G_{ft} = 6 \times (f_{cm})^{0.7} \quad (26)$$

Figure 4 shows that pre-peak relationship obtained with the three models is similar, but when tension softening starts, the Hillerborg model leads to an abrupt decrease of stress. On the other hand, the softening branch of the modified Mazars model tends to approximate the one obtained with MC2010 at late stages of post-cracking (strains larger than  $0.4\text{‰}$ ). Therefore, it is possible to state that the proposed model presents a valid similarity with the one provided in MC2010. The main advantage of this model, is that it does not present any derivative discontinuity, which can enable added numerical stability during the iterative process required by the solution of the non-linear governing systems.

It is expected that models with tension stiffening present a less pronounced transition from phase I, uncracked, to phase II cracked. This will be observed in the reinforced beam example presented in section 6.5.

Eqs. (25) and (26) were used to estimate the tensile fracture energy since these expressions are consensual and used without reservations by designers and researchers for the numerical modelling of the mechanical behaviour of common concrete compositions. However, since both expressions are empirical and depend only on the compressive strength, relevant differences between the estimates of Eq. (25) and (26) and the actual value of fracture energy may occur.

Fracture energy is mostly dependent on the strength of the coarse aggregates, on their content, on the maximum aggregate diameter, and on the water / binder ratio [50]. Since the water / binder ratio will affect both compressive strength and fracture energy, the accuracy of Eqs. (25) and (26) will not be relevantly affected whenever this parameter deviates from usual mix design. However, since Eqs. (25) and (26) are empiric, whenever any of the aforementioned parameters related to coarse aggregates are largely different from common concrete compositions, Eqs. (25) and (26) may not be applicable.

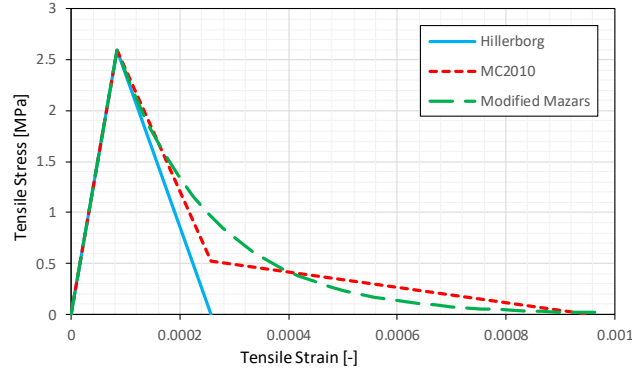


Figure 4 – Tensile Stress vs Tensile Strain.

Therefore, the authors recommend specific testing whenever: 1<sup>st</sup> the maximum aggregate diameter is either larger than 25 mm or smaller than 16 mm (the case of the benchmark presented in Section 6.1); 2<sup>nd</sup> the content of aggregates differs from common; 3<sup>rd</sup> weak aggregates are used, such as recycled aggregates or lightweight aggregates [51]. Weaker aggregates will be associated with clean and planar fracture surfaces, with relevant amount of trans-aggregate fractures [52], decreasing fracture energy.

## 5.2 Compressive Behaviour

Typically, commercial finite element software does not use fracture energy regularization for the stress-strain relationship defining concrete behaviour under compression. To the authors best knowledge, this is due to the lack of consensus on how to determine the compressive fracture energy. In this section, the compressive stress vs strain diagram obtained with the proposed modified Mazars damage model is directly compared with the corresponding curve defined in MC2010 [12]. This comparison is presented in Figure 5 and four different estimates for the compressive fracture energy are considered in the definition of the modified Mazars damage model [33]. These estimates were chosen after appraising the state-of-the-art regarding this subject. The following constitutive models for the compressive strength vs. compressive fracture energy relationship were compared [40, 45, 53, 54]:

$$\begin{cases} G_{fc-A} = 8.8\sqrt{f_{cm}} \\ G_{fc-B} = 250 \times G_{ft} \\ G_{fc-C} = 8.6 \times f_{cm}^{0.25} \\ G_{fc-D} = \left(\frac{f_{cm}}{f_{ctm}}\right)^2 \times G_{ft} \end{cases} \quad (27)$$

The compressive constitutive law proposed in MC2010 is well-approximated when the estimate given by  $G_{fc-C}$  is used. Therefore, in the following examples  $G_{fc-C}$  is always assumed, unless stated otherwise.

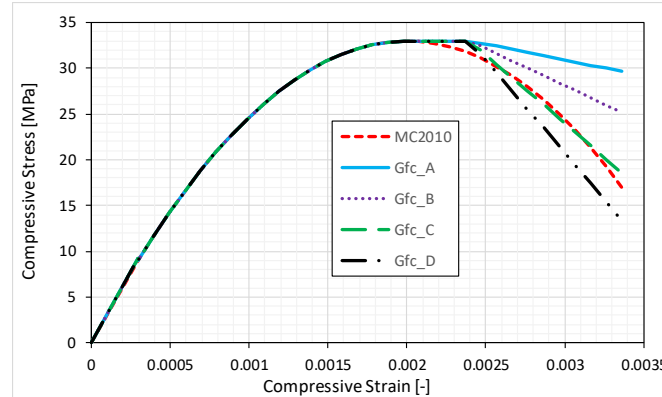


Figure 5 – Compressive Stress vs Compressive Strain.

As in the case of the tensile fracture energy, two of the expressions presented in Eq. (27) depend on the compressive strength only; therefore, the recommendations made in the last section for specific testing are also applicable here. Concrete compositions that differ from usual may not be as erroneously estimated when either of expressions  $G_{ffc\_B}$  or  $G_{ffc\_D}$  are used (provided  $G_{ft}$  and  $f_{ctm}$  are tested). However, hypothesis cannot be confirmed, because the compressive fracture energy is very rarely tested and is strongly dependent on test setup (e.g. on differences regarding specimen shape and boundary restraints [55]).

## 6 Numerical Examples

In this section, five well known and widely used benchmark tests are considered. The modified Mazars damage model was implemented via user subroutine UMAT using Standard Fortran in the commercial software ABAQUS Standard. The results obtained with the model being proposed are compared with previous experiments in terms of global structural response and, when possible, in terms of crack distribution. In all examples the fracture energy regularization is considered, and according to the theory presented in [56], viscous regularization with  $\eta = 10^{-5}$  is used to prevent convergence issues [57]. All finite element meshes consider 4-node bilinear elements with reduced integration and hourglass control. All structures are analysed considering 2D models and with symmetry simplifications whenever possible to reduce computational cost. For the solution of the non-linear governing system, the predictor-corrector based on the use of a secant stiffness matrix is used.

When the secant stiffness matrix is used in a classical predictor-corrector algorithm, the iterative process is more severe, and some convergence controls used in classical Newton-Raphson with tangent matrix must be eased. Therefore, the default general solution controls of ABAQUS must be modified. To prevent severe cut backs in the iterative incremental process, a minimum of 100 iterations are needed for each time load. To promote iterative numerical stability, the maximum displacement increment in every node is limited to 10%, and ABAQUS “discontinuous analysis” is used. This will increase the total need of iterative steps, but provides an accurate final converged solution. To allow for the simulation of softening behaviour, displacement control is considered in all test cases.

### 6.1 The Hassanzadeh Test

The first example is a known benchmark test, used to assess concrete damage models. It is known as the “Hassanzadeh Test” [58], in which a plain concrete specimen with four edge notched is tested under monotonic static tension, using displacement control until a maximum displacement of 0.04 mm in the

top of the specimen (Figure 6). Similarly to other published works [59], the numerical model is simplified adopting a 2D analysis, by idealizing a plane strain hypothesis. It was reported in [58] that concrete presents a cubic compressive strength of  $f_{cm} = 50MPa$ , and using the constitutive models of MC2010, the tensile strength is estimated as  $f_{ctm} = 3MPa$  and the secant Young modulus as  $E_{cm} = 35GPa$ . Although the original author did not provide the exact value of the tensile fracture energy of their experiment, several authors have proposed values ranging from 50N/m to 73.35N/m [60, 61]. In this paper an average value of 62N/m is used, since the values of MC2010 are not adequate for concrete with small aggregate dimensions (smaller than 9 mm) - see Sections 5.1 and 5.2.

As suggested by other authors [59], the forces associated with the prescribed displacements at the top surface obtained with this 2D analysis have to be corrected to take into consideration the 3D effect of the problem.

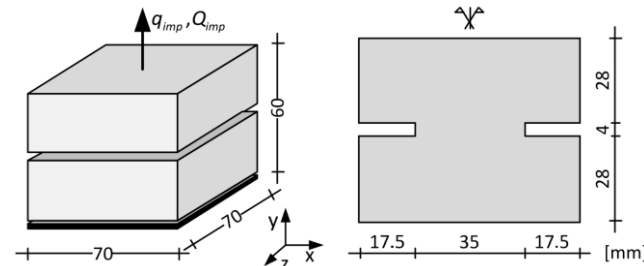


Figure 6 – Hassanzadeh test geometry [61].

To evaluate mesh dependency when using fracture energy regularization, a regular mesh was refined three times using a meshing algorithm with maximum element size ranging from 1.5mm to 0.5mm. To correct mesh non-conformity, a kinematic constraint is applied at the interface between the coarse mesh (general regions of the specimen) and the refined mesh (near the notches of the specimen). Although a non-conforming interface may exist, no  $C^0$  violation occurs, and the problem is displacement-compatible. In every case the mesh is refined homothetically throughout the whole domain. To reduce computational cost, symmetry conditions have been considered Table 1.

Figure 8 displays the final tension damage distribution obtained for the three meshes shown in Figure 7. It is possible to observe that crack damage region is similar in all three discretization meshes tested, and localized in a band with finite length, as expected when fracture energy regularization is used. Figure 9 shows the tension damage evolution for several load steps. In all cases a distributed damage near the notched edges may be observed.

Table 1 – Mesh Refinement for the Hassanzadeh test.

| Mesh Name                        | A   | B   | C    |
|----------------------------------|-----|-----|------|
| Number of FE in the notched edge | 3   | 4   | 8    |
| DOF                              | 104 | 360 | 1334 |



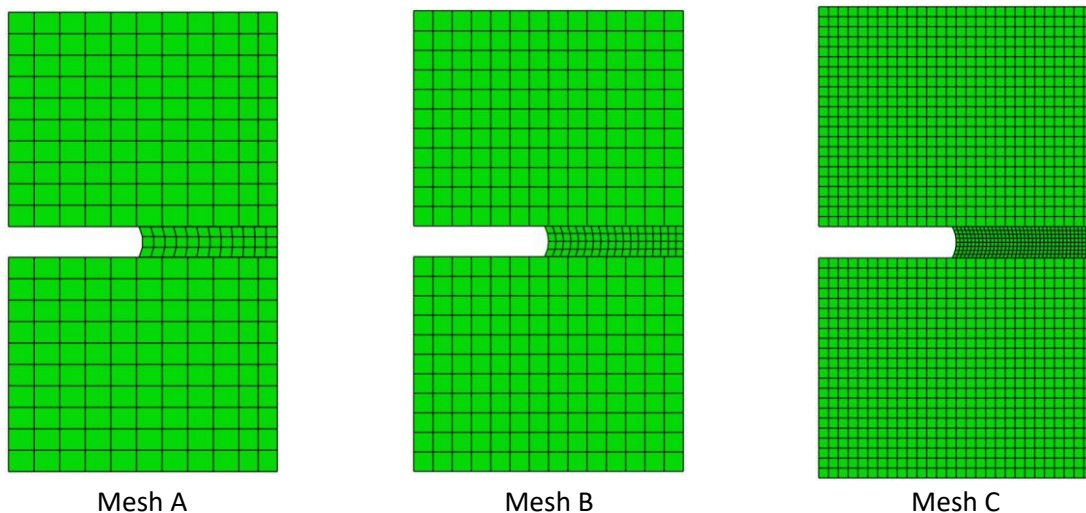


Figure 7 – Adopted meshes for the Hassanzadeh Test.

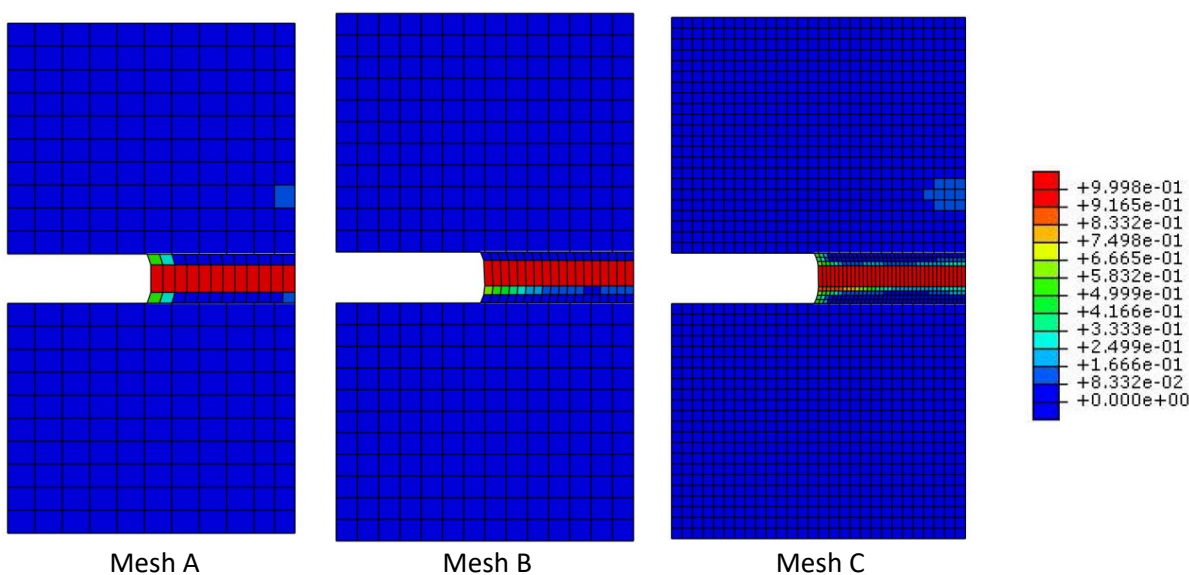


Figure 8 – Final tension damage distribution for each discretization (deformed shape).

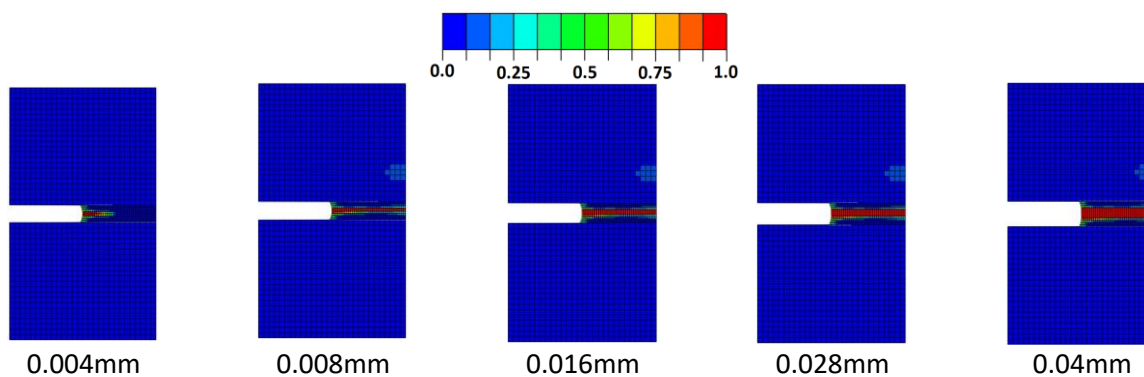


Figure 9 – Tension damage evolution for mesh C.

Figure 10 shows the reaction vs vertical displacement structural response obtained with all tested discretizations. The experimental curve is also plotted and it is verified that the global structural response is quite similar in all cases. Therefore, it can be concluded that no mesh dependency occurs and objective solutions are always achieved. Figure 10 also shows that mesh C leads to a very similar structural behaviour when compared to the experimental data provided by [58]. The bump experimentally observed in the softening branch is due to rotational instability occurring when the test apparatus has a low rotational stiffness [49, 58]. Therefore, this is not present in the numerical simulations, since equal displacements are imposed to all points on the top surface of the specimen. Also as expected, due to impose displacements, the stiffness of the coarse mesh is smaller.

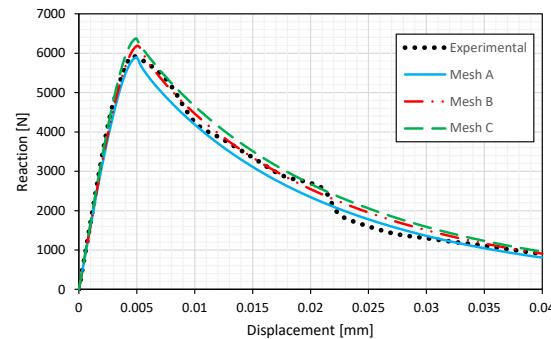


Figure 10 – Reaction vs vertical displacement diagrams obtained in the analysis of the Hassanzadeh test.

## 6.2 The L-shaped Panel Static Test

The L-shaped panel has become a popular benchmark test for the validation of computational models used in the numerical simulation of plain concrete cracking. In order to provide experimental data, tests on L-shaped structural members were performed at the University of Innsbruck [62]. The test setup, geometric properties, and boundary conditions are shown in Figure 11. An upward maximum vertical displacement of 1.0mm is prescribed at the lowest right corner of the structure. Young's modulus, Poisson's ratio, the cylindrical compressive strength, the uniaxial tensile strength and fracture energy are given by  $E = 26 \text{ GPa}$ ,  $\nu = 0.18$ ,  $f_c = 31 \text{ MPa}$ ,  $f_t = 2.5 \text{ MPa}$  and  $G_f = 90 \text{ N/m}$ . As in the previous example, the adopted fracture energy value is clearly smaller than the one provided by MC2010. This value is adopted since it was measured by the original author for the case of concrete with small aggregates.

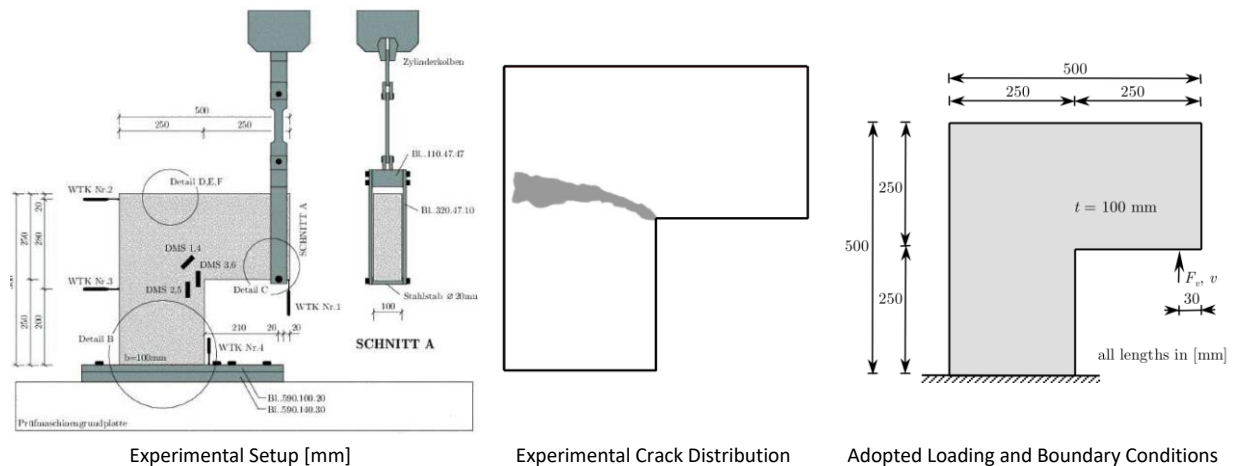


Figure 11 – Force vs vertical displacement from L-shaped panel static test [62].



The three regular structured meshes shown in Figure 12 are considered in the analysis Table 2. To prevent any localized effects associated to the application of the prescribed displacement, a linear elastic behaviour is adopted for the material localized near the right boundary of the L-shaped plate.

Table 2 – Mesh Refinement for the L-shaped Panel Static test.

| Mesh Name      | A   | B    | C     |
|----------------|-----|------|-------|
| FE square size | 25  | 12   | 5     |
| DOF            | 682 | 2562 | 15402 |

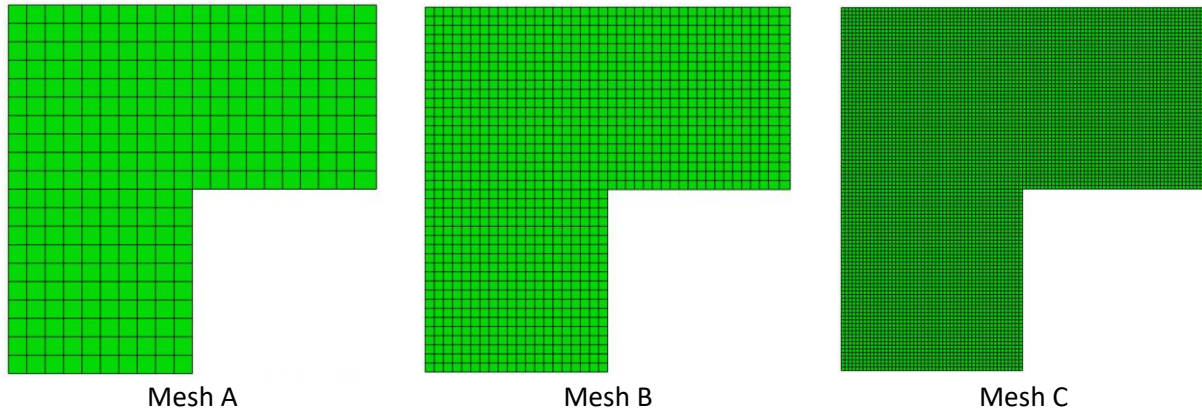


Figure 12 – Adopted meshes for the L-shape panel.

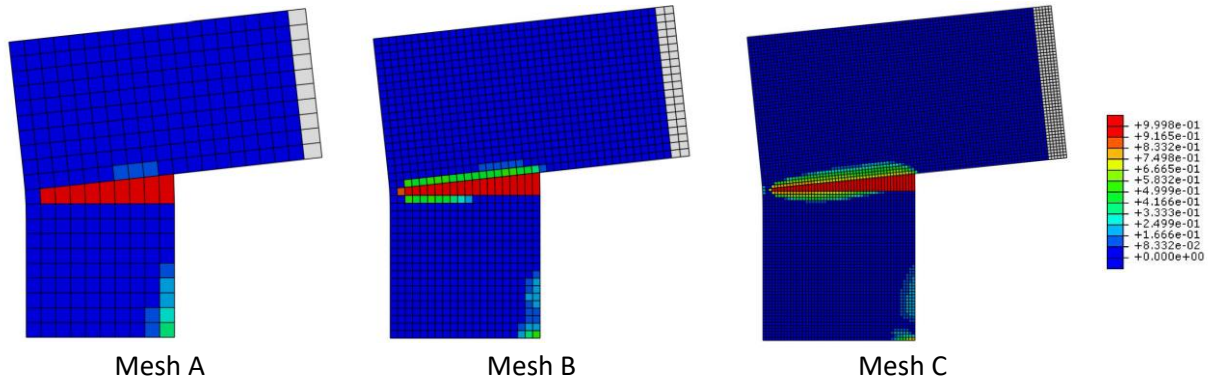


Figure 13 – Final tensile damage distribution (deformed shape).

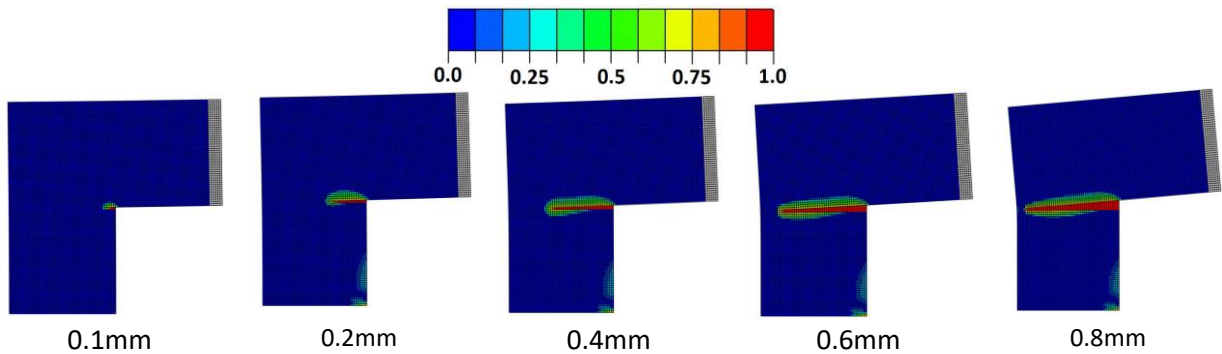


Figure 14 – Tensile damage evolution when Mesh C is used.

Figure 13 shows the final tension damage distribution obtained with all discretizations being considered. As it can be observed, the localized damage band is stable and does not depend on the size of the elements considered in the mesh. The evolution of the tensile damage distribution for several load step increments is plotted in Figure 14. As expected, damage first appears near the re-entrant corner and then evolves almost horizontally, correctly simulating the development of a macro-crack.

The force vs vertical displacement structural response obtained with the discretization being used are plotted in Figure 15. Two experimental curves are also included in the same plot. It can be seen that objectivity is ensured, as global structural responses are quite similar and are not mesh dependent. It is important to note that in all numerical solutions that have been obtained, the stiffness and maximum load, although identical, are not equal to the experimental results. This has been pointed out by other authors, and it is due to some uncertainty related to the support conditions of the experimental test. Also, a minor crushing in the concrete near the load metal plate was observed, which promotes a more flexible and structural response with less load-bearing capacity. Due to the non-linearity started at the first steps, in this particular case, it is expected that the coarser mesh is stiffer.

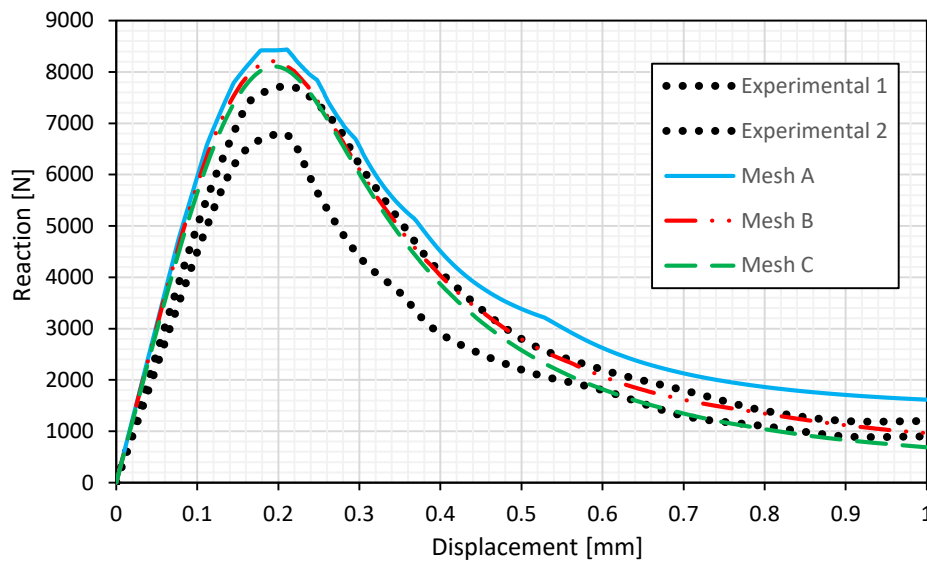


Figure 15 – Force vs vertical displacement from L-shaped plate.

### 6.3 Four-Point Bending Test

This example reproduces a recent benchmark, in which a four-point bending test is performed to estimate the fracture energy in a concrete beam (Figure 16). This test was reported for the first time in [63], in which the authors concluded that in this type of experimental setup there is almost no size effect in the measurement of fracture energy. This example is important because it evaluates fracture energy in a pure bending region, thus removing any shear effect that may cause a portion of the size effect. The crack-depth is 40 mm and has a thickness of 3 mm, and a prescribed displacement is applied in the top steel plates. The properties are provided by the original authors: Young modulus  $E_{cm} = 32.46 \text{ GPa}$ ; cylindrical compressive mean strength  $f_{cm} = 32.4 \text{ MPa}$ ; the tensile strength  $f_{ctm} = 2.5 \text{ MPa}$  was estimated using MC2010; and the tensile fracture energy  $G_{ft} = 190 \text{ N/m}$  (similar to the one in MC2010).

To reduce the computational cost, symmetry considerations and a localized refined mesh are adopted. As shown in Figure 17 a), the refined mesh is located near the notched edge and a kinematic constraint is considered at the transition zone in order to promote  $C^0$  continuity at the interface. A sweep mesh was defined in the refined area using an advancing front algorithm, promoting a total

1554 DOF. This ensured that at least three elements exist in the notched edge, as it can be verified in Figure 17 b). The length of this localized refined mesh is based on an initial iterative approach using a simple elastic numerical model.

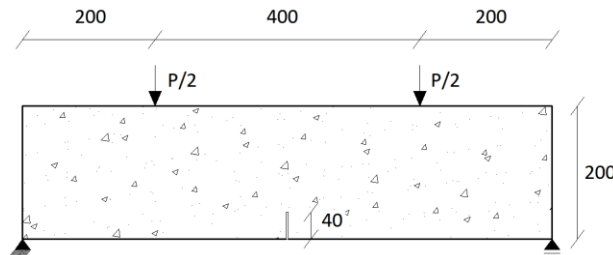
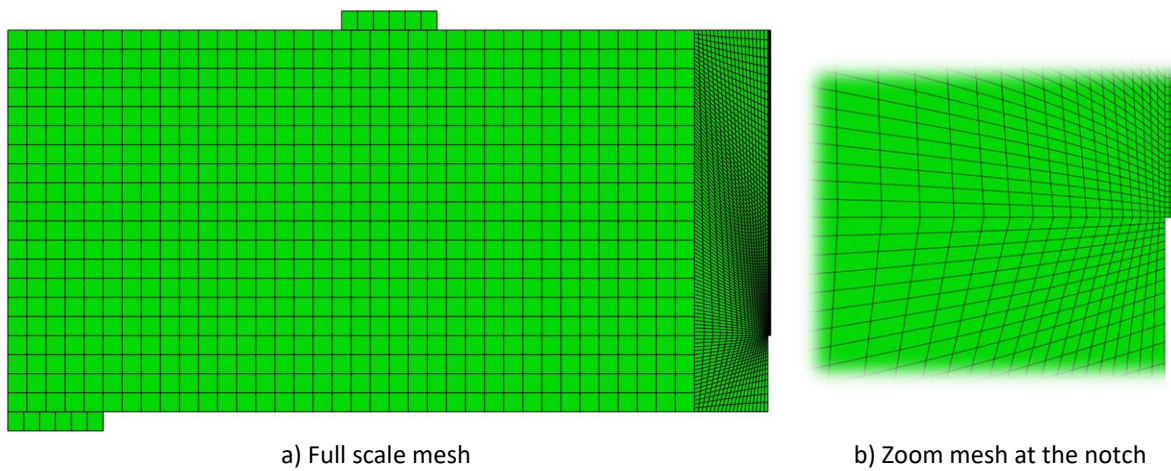


Figure 16 – Four-point bending test setup [mm].



a) Full scale mesh  
b) Zoom mesh at the notch  
Figure 17 – Adopted mesh for the four-point bending test.

Figure 18 shows the tensile damage evolution near the notch for different load steps. To ensure a better visualization of the results, the mesh grid is removed. As expected, damage first appears near the notched edge and evolves along the height of the crack.

Figure 19 shows the evolution of the maximum principal positive stress. The maximum principal positive stress value does not progress towards the top of the specimen at the final stages of the loading process.

Figure 20 plots the reaction vs displacement structural response obtained with the constitutive model being presented. This figure shows also two curves obtained with experimental tests. It can be observed that the numerical response with the material parameters provided by the original authors [63] is consistent with the upper and lower experimental data in turns of force reaction. For the stiffness, although the original authors state no crushing in the supports, it is possible that some experimental results may be more flexible due to this problem.

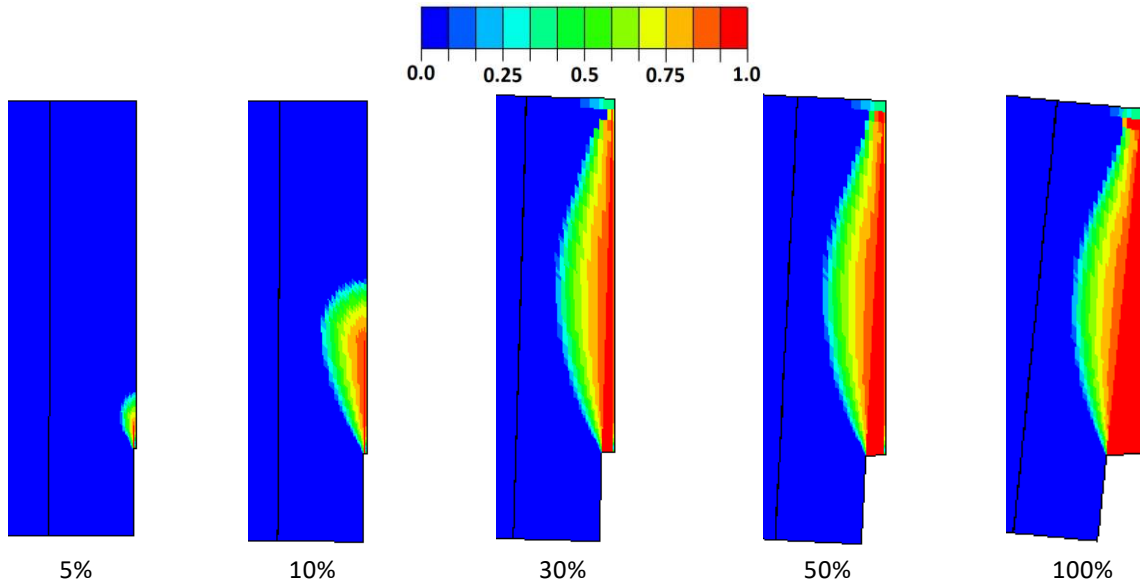


Figure 18 – Tensile damage evolution for a % of 1.0mm of displacement at the top  $\frac{1}{2}$  span.

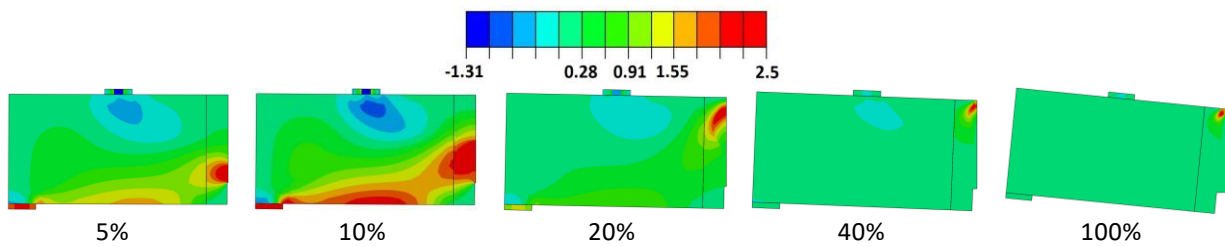


Figure 19 – Maximum positive stress for a % of 1.0mm of displacement at the top  $\frac{1}{2}$  span.

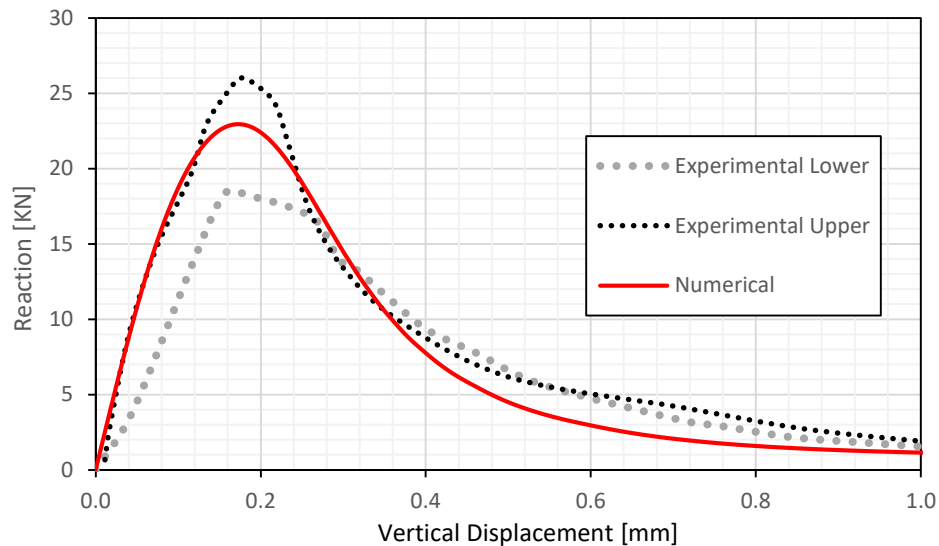


Figure 20 – Force vs displacement in the four-point bending test.



#### 6.4 Skew Crack in a Compression Field

The main purpose of this benchmark is to validate the compressive fracture energy regularization formulas presented in (27), and also verify if the damage model works correctly during compressive damage. This experiment was first reported in [64], and the only material parameter directly provided by the authors is the mean compressive strength,  $f_{cm} = 25 \text{ MPa}$ . The authors of the publication inferred the compressive fracture energy indirectly and observed that their estimates were too wide and unreliable, therefore these data were not used. The remaining necessary material parameters are estimated using MC2010: secant Young Modulus  $E_{cm} = 27 \text{ GPa}$ ; cracking stress  $f_{ctm} = 2.0 \text{ MPa}$ ; and tensile fracture energy  $G_{ft} = 130 \text{ N/m}$ . In this example the four alternative expressions defined in equation (27) for the computation of the compressive fracture energy are tested and the results obtained with those alternative values are compared.

It is important to point out that the length of the notched edge and the complete information regarding the structural response of the concrete prism are not presented in the original publication [64]. Therefore, assumptions were required in order to have all necessary geometric information. Based on the information provided by the drawings in the original paper [64], the length of the notch was estimated to be 38 mm.

The load is applied at the top of the specimen and correspond to a uniform prescribed vertical displacement, using an irregular mesh with a total of 20836 DOF.

Figure 21 shows the experimental crack paths that have been reported in [64]. That paper presents the crack patterns obtained when an inclination of  $45^\circ$  is considered for the notch, but then presents the global structural response only for the case in which that inclination corresponds to  $30^\circ$ .

In the numerical simulation presented in this section, an inclination of  $30^\circ$  is considered to enhance the comparison of the global structural behaviour. The maximum positive principal strain distribution obtained with the numerical model is presented in Figure 21 for different stages of the loading process. A very good agreement between both numerical and experimental results is observed.

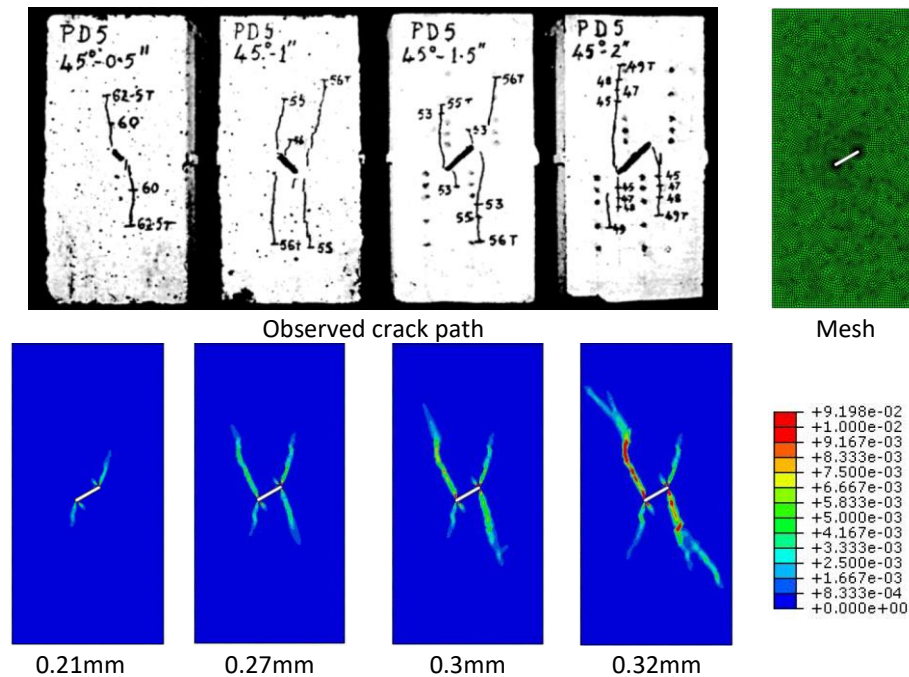


Figure 21 – Experimental crack path in specimens and numerical maximum positive principal strain, for a given vertical prescribed displacement.

Figure 22 a) shows the vertical top reaction vs displacement structural response that are obtained when the four alternative expressions presented in equation (27) for the definition of the compressive fracture energy are taken into account. The experimental curve is also plotted in the same figure, in which the original author stopped the load at 0.24mm in order to photograph the crack patterns. It is possible to observe that all four numerical curves present the same peak load and that both numerical and experimental results are quite similar. As expected, if one takes into consideration the comments presented in section 5.2, the numerical simulation with  $G_{fc\_A}$  presents higher ductility. By observing the experimental curve and the numerical structural response obtained with  $G_{fc\_C}$ , it can be concluded that non-linearity is similar, although the finite element model was only able to reach a maximum vertical force of 382 kN at 0.32 mm. Figure 22 b) presents the final damage distribution obtained with a compressive fracture energy value given by expression  $G_{fc\_C}$  in equation (27), and it can be observed an onset of collapse, on both lateral sides, that promote the softening at 0.32mm.

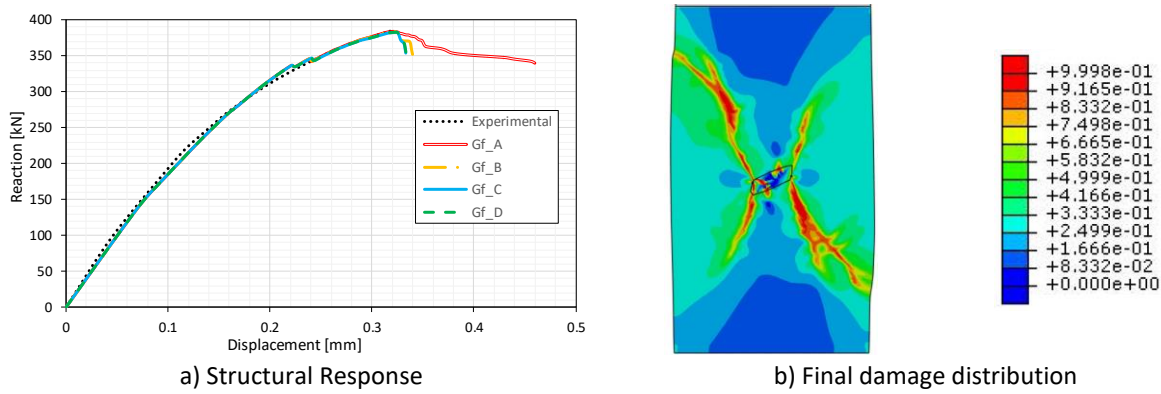


Figure 22 – Force vs displacement in the skew-crack test, and final damage distribution (deformed shape).

## 6.5 Reinforced Concrete Beam

This last example tests the accuracy of the proposed modified Mazars damage model in the simulation of the behaviour of a reinforced concrete beam in which the collapse is due to concrete compression. Therefore, this is an important numerical benchmark to test the regularization technique associated to compressive fracture energy. Most of the material parameters are provided in [65, 66]: Young modulus for concrete  $E_{cm} = 31 \text{ GPa}$ ; cylindrical compressive strength  $f_{cm} = 37 \text{ MPa}$ ; Young modulus for steel and hardening stiffness,  $E_s = 193 \text{ GPa}$ ;  $E_{sy} = 10\% E_s$ , respectively; yield and ultimate steel stress  $f_y = 546 \text{ MPa}$ ;  $f_{yu} = 691 \text{ MPa}$ . For the steel reinforcement an elastoplastic model with constant stress after hardening value is used. Since the damage model in this work is based on the constitutive relations of MC2010, the concrete cracking stress was considered to be  $f_{ctm} = 2.8 \text{ MPa}$  and the fracture energy  $G_{ft} = 140 \text{ N/m}$ .

Although the original authors have used a full 3D finite element analysis, for the simulation presented in this work a simple 2D analysis is performed to reduce the computational costs, since it was observed during the experimental campaign that out of plane effects were irrelevant. The reinforced concrete section and load layout are presented in Figure 23, but more information on the structural setup can be found in [67], in which a maximum prescribed displacement 30 mm is applied in the top steel plates.

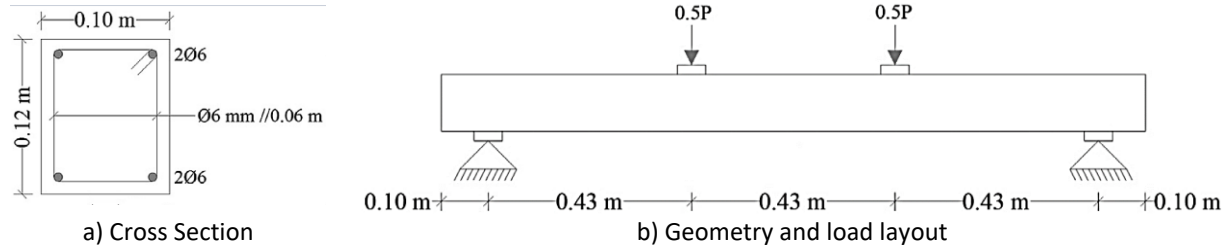


Figure 23 – Load layout of the reinforced concrete beam [65, 67].

The finite element size is limited to 5 mm for plane and rebar elements, in which more detailed information is presented in [65], with a total of 7500 DOF. For the rebar elements, truss 2 node finite elements are used and perfect bond to the concrete is assumed.

Three different numerical models involving the use of the finite element mesh presented in Figure 24 are considered in the analysis of the reinforced beam. The first, designated as Numerical Model A, considers the values above mentioned for all parameters characterizing the material behaviour. A second model, designated here as Numerical Model B, uses the value for the tensile fracture energy defined by Hillerborg [49]. Finally, Numerical Model C takes into account the branch AB defined in Figure 2 ( $\varepsilon_{t1} \neq \varepsilon_{d0}$ ).

Figure 24 shows the force vs displacement (at mid span) structural response obtained with all three numerical models defined above. The same figure shows the experimental results and the analytical solution that can be obtained using the standard MC2010 design equations.

The analysis of Figure 24 shows a difference between numerical and experimental results in the transition from phase I to phase II after cracking initiation. As the numerical solutions are quite similar to the analytical one, this difference may be related to some defects of the specimen, originated during production or transportation, that caused premature cracking.

When comparing the experimental and numerical values obtained for the cracking bending moment and corresponding load, close agreement is found. The bending cracking moment is approximately  $M_{cr} = 1.5 \text{ kNm}$  and the load is about  $P_{cr} = 7.14 \text{ kN}$ .

Figure 24 shows that the stiffness associated to phase II computed using the MC2010 procedure is well recovered by all numerical models. However, phase II maximum load obtained with Numerical Model A and Numerical Model C overestimate the analytical value. When Numerical Model B is considered that difference tends to decrease.

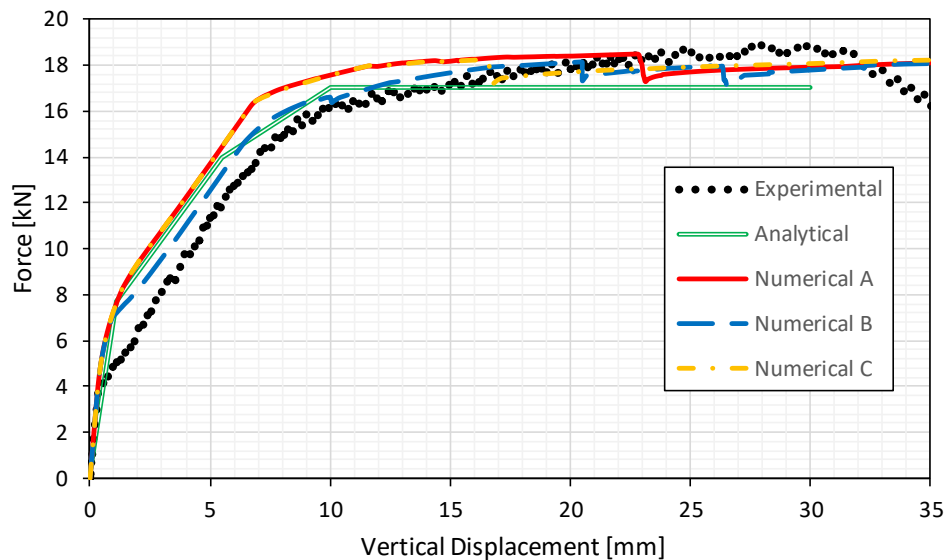


Figure 24 – Force vs displacement at mid span of the reinforced concrete beam.

This damage model allows the user to identify if the material is closer to a tension or compression state by plotting both  $\alpha_T$ ,  $\alpha_C$  variables (defined in equation (16)). Figure 25 shows, as expected, that the tensile behaviour is mostly located in the middle and bottom of the specimen, while compressive behaviour is located at the top.

Figure 26 presents the damage distribution obtained for different stages of the loading process. For each diagram the value of the displacement being prescribed is indicated. The maximum value considered for the prescribed displacement is 30 mm and all diagrams are presented considering the beam deformed shape.

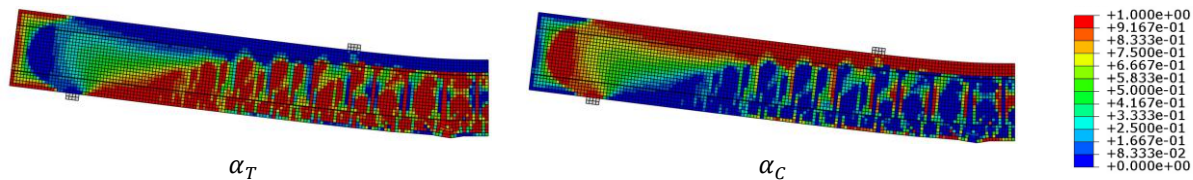
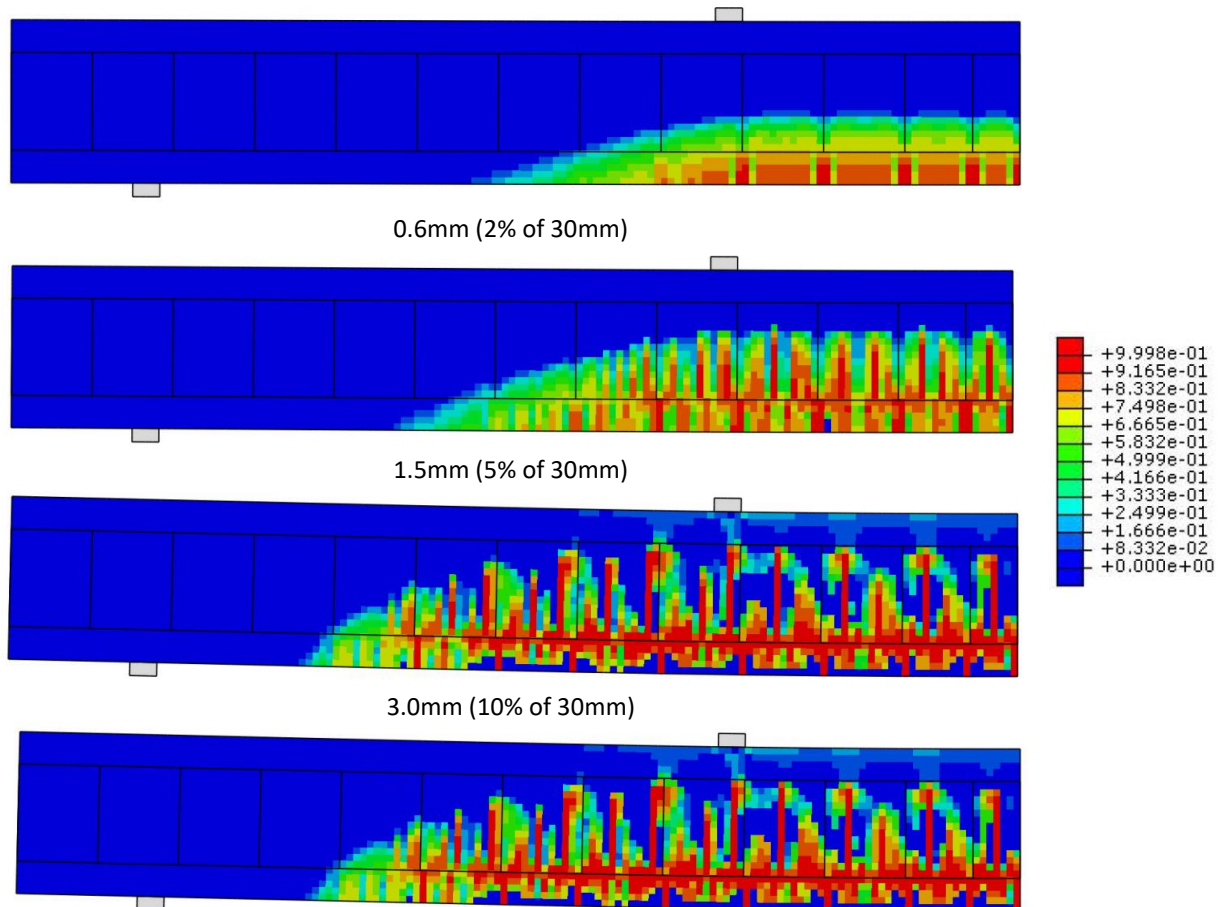


Figure 25 – Tensile and compressive factors for tensile and compressive damage combination.

In Figure 26, the displacement of 0.6 mm (2% of 30 mm) represents the transition from elastic behaviour to the cracking phase (which is finished at 5% of 30 mm). Then, the beginning of the yielding of the rebars and crushing of the concrete occurs at 17% and 55% of the maximum displacement, respectively. As in the experimental outputs described in [65, 67], the beam presented a huge crack near the load support due to steel rebar yielding (Figure 27) and a clear concrete crushing near the top of the beam at half span.





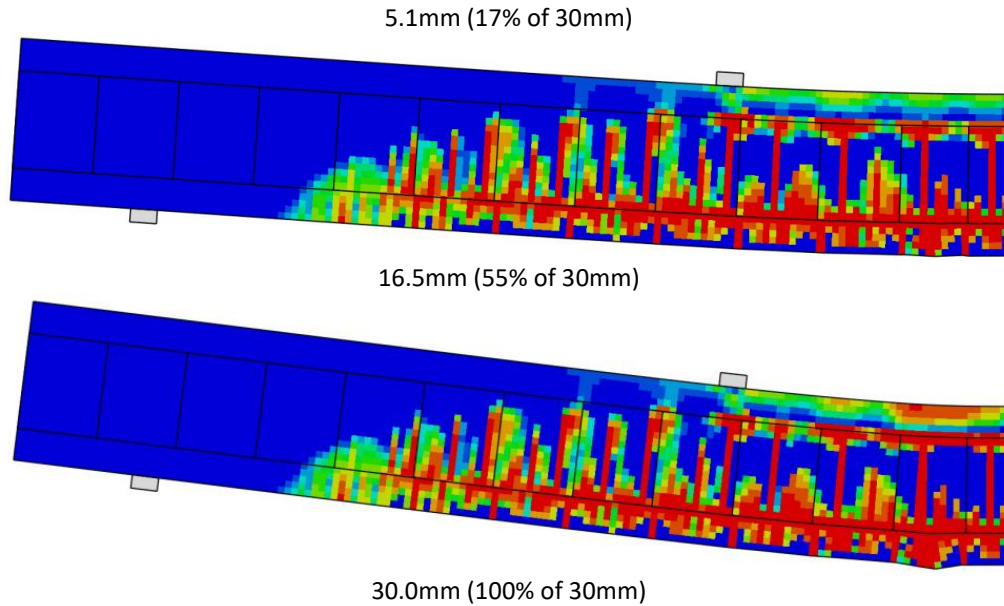


Figure 26 – Damage distribution for different phases of the loading process.

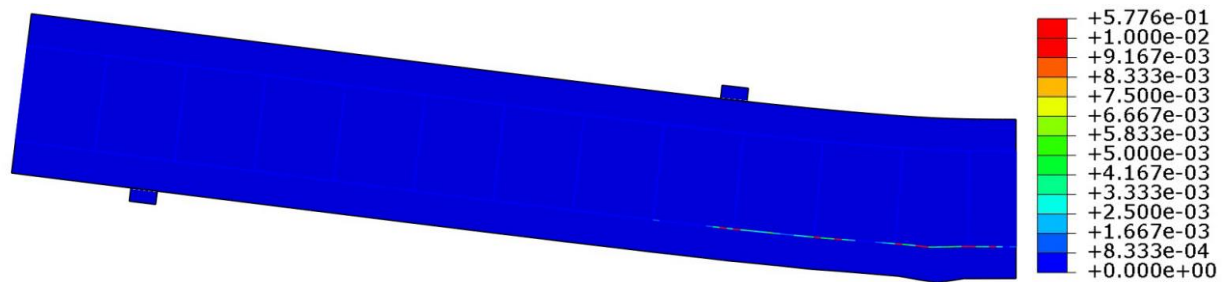


Figure 27 – Final plastic strain in the steel rebars.

## 7 Conclusions

In this work a new modified Mazars damage model has been presented and tested. This new model defines the damage evolution laws according to Model Code 2010. A comprehensive set of numerical tests were performed considering well-known benchmark examples currently used to assess damage models. In the examples discussed in this paper, the results obtained with the model being proposed are compared with experimental results in terms of global structural response and crack pattern distribution. The main conclusions of this work are:

- 1) The proposed damage model was able to simulate previous experimental campaigns in terms of force vs displacement curves both in tension and compression. Accurate results in terms of non-linear stiffness and maximum load capacities have also been reported;
- 2) The model is able to correctly simulate the crack patterns observed in experiments;
- 3) Due to the energy regularization of both tensile and compressive damage, the proposed model did not present any mesh dependency or sensitivity. This was the main goal to achieve with the development of this new model;
- 4) Although simple in terms of formulation and damage evolution laws, the model leads to robust and accurate results. Moreover, the model is computationally efficient.

Another important secondary conclusion is that, the tensile damage evolution was compared and validated with previous authors and good agreement was observed, when using fracture energy regularization. For the compressive damage evolution four formulas that estimate the compressive fracture energy were tested, and all of them were directly compared with stress vs strain curves of MC2010. The relationship labelled in the paper as  $G_{fc}-C$  [45] resulted in the best fit of the model to the benchmark data. In any case, it was possible to concluded that the four compressive fracture energy analytical formulas, although different, produce similar numerical results.

## 8 Future Developments

In the near future the modified Mazars model will be upscaled in order to allow for the correct and accurate simulation of both static and dynamic cyclic analysis. To perform this, permanent strains and hysteretic loops must be added to the formulation by means of gradient functions. The proposed damage model will also be generalized to enable statistical variation of material properties, which is an important issue when considering of the variability of secondary raw materials for concrete, an increasingly relevant trend of the concrete industry.

## 9 Acknowledgements

This work has been partly supported by Fundação para a Ciência e Tecnologia, under the Transitional Standard – DL57/2016/N3/UI/CERIS/CT/165/2018.

## 10 References

- [1] Bazant ZP, Cedolin L. Stability of structures: elastic, inelastic, fracture, and damage theories: Oxford University Press, 1991.
- [2] Carpinteri A. Mechanical damage and crack growth in concrete: plastic collapse to brittle fracture. 1st edition ed: Martinus Nijhoff Publishers, 1986.
- [3] Jirásek M. Nonlocal models for damage and fracture: comparison of approaches. International Journal of Solids and Structures. 1998;35:4133–45.
- [4] Cirak F, Ortiz M, Pandolfi A. A cohesive approach to thin-shell fracture and fragmentation. Computer Methods in Applied Mechanics and Engineering. 2005;194\;:2604-18.
- [5] Borst R, Gutiérrez MA, Wells GN, Remmers JJC, Askes H. Cohesive-zone models, higher-order continuum theories and reliability methods for computational failure analysis. International Journal for Numerical Methods in Engineering. 2004;60:289-315.
- [6] Planas J, Elices M. Asymptotic analysis of a cohesive crack: 1. Theoretical background. International Journal of Fracture. 1992;55:153-77.
- [7] Planas J, Elices M. Asymptotic analysis of a cohesive crack: 2. Influence of softening curve. International Journal of Fracture. 1993;64:221-37.

- [8] Stolarska M, Chopp DL, Moes N, Belytschko T. Modelling crack growth by set levels in the extended finite element method for cohesive crack growth. *International Journal for Numerical Methods in Engineering*. 2001;51:943-60.
- [9] Ibijola EA. On some fundamental concepts of Continuum Damage Mechancis. *Computer Methods in Applied Mechanics and Engineering*. 2002;191:1505-20.
- [10] Krajcinovic D. *Damage Mechanics*. North-Holland1996.
- [11] Mazars J, Walter D. *Endommagement mecanique du beton*. France1980.
- [12] FIB. The fib Model Code 2010 for Concrete Structures, Model Code. International Federation for Structural Concrete. In: Sohn E, editor. Switzerland, Lausanne: FIB; 2010.
- [13] Pijaudier-Cabot G, Mazars J. SECTION 6.13 - Damage Models for Concrete. In: Lemaitre J, editor. *Handbook of Materials Behavior Models*. Burlington: Academic Press; 2001. p. 500-12.
- [14] Deusdado N, Antão AN, Silva MVd, Guerra N. Application of the Upper and Lower-bound Theorems to Three-dimensional Stability of Slopes. *Procedia Engineering*. 2016;143:674-81 DOI: <https://doi.org/10.1016/j.proeng.2016.06.097>.
- [15] Mazars J, Hamon F, Grange S. A new 3D damage model for concrete under monotonic, cyclic and dynamic loadings. *Materials and Structures*. 2015;48(11):3779-93 DOI: 10.1617/s11527-014-0439-8.
- [16] Falco AD, Mori M, Sevieri G. Mazar damage model for masonry structures: a case study of a church in Italy. *COMSOL Conference 2018*. Lausanne2018.
- [17] Task-Group-4-4. Bulletin 45 - Practitioners' guide to finite element modelling of reinforced concrete structures In: (fib) IFfSC, editor. Bulletin 45. Lausanne2008.
- [18] Kachanov M. On the time to rupture under creep conditions. *Izvestija Akademii Nauk SSSR, Otdelenie Techniceskich Nauk*. 1958;8:202-18.
- [19] Rabotnov YN. Creep Rupture. 12th International Congress of Applied Mechanics. Stanford1968.
- [20] Lemaitre J. *A Course on Damage Mechanics*. Verlag: Springer, 1992.
- [21] Lemaitre J, Chaboche JL. *Mécanique des matériaux solides*: Dunod, 1985.
- [22] Lemaitre J, Desmorat R. *Engineering Damage Mechanics*. Berlin Heidelberg: Springer, 2005.
- [23] Lee J, Fenves GJ. Plastic-damage model for cyclic loading of concrete structures. *J Eng Mech ASCE*. 1998;124:892-900.
- [24] Pires FMA, César de Sá JMA, Sousa LC, Jorge RMN. Numerical modelling of ductile plastic damage in bulk metal forming. *International Journal of Mechanical Sciences*. 2003;45(2):273-94.
- [25] ABAQUS. Abaqus Unified FEA-3DEXPERIENCE R2018. In: Systèmes D, editor. Rhode Island: 3DS-SIMULIA; 2018.

- [26] Abu-Obeidah A, Hawileh RA, Abdalla JA. Finite element analysis of strengthened RC beams in shear with aluminum plates. *Computers & Structures*. 2015;147:36-46 DOI: <https://doi.org/10.1016/j.compstruc.2014.10.009>.
- [27] Hawileh RA, Naser MZ, Abdalla JA. Finite element simulation of reinforced concrete beams externally strengthened with short-length CFRP plates. *Composites Part B: Engineering*. 2013;45(1):1722-30 DOI: <https://doi.org/10.1016/j.compositesb.2012.09.032>.
- [28] Hawileh RA, Rahman A, Tabatabai H. Nonlinear finite element analysis and modeling of a precast hybrid beam-column connection subjected to cyclic loads. *Applied Mathematical Modelling*. 2010;34(9):2562-83 DOI: <https://doi.org/10.1016/j.apm.2009.11.020>.
- [29] Hawileh RA, El-Maaddawy TA, Naser MZ. Nonlinear finite element modeling of concrete deep beams with openings strengthened with externally-bonded composites. *Materials & Design*. 2012;42:378-87 DOI: <https://doi.org/10.1016/j.matdes.2012.06.004>.
- [30] Geers MGD. Continuum Damage Mechanics. In: 4K060 In-c, editor. 1999.
- [31] Pijaudier-Cabot G, Benallal A. Strain localization and bifurcation in a nonlocal continuum. *International Journal of Solids and Structures*. 1993;30:1761-75.
- [32] Bazant ZP, Oh BH. Crack band theory for fracture of concrete. *Materials and Structures*. 1983;16:155-77.
- [33] Mazars J. J.. Application de la mécanique de l'endommagement au comportement non lineaire et à la rupture du béton de structure. Paris: Université Paris 6, Ph.D Thesis, 1984.
- [34] Code\_Aster/Salome-Meca. Analyses des Structures et Thermomécanique pour des Études et des Recherches. France: Code\_Aster, 2020.
- [35] Polanco-Loria M, Sorensen SI. Damage Evolution Laws for Concrete - Comparative Study. In: Wittmann FH, editor. *Fracture Mechanics of Concrete Structures, Proceedings FRAMCOS-2*. D-79104 Freiburg: AEDIFICATIO Publishers; 1995.
- [36] Donath S, Iglberger K, Wellein G, Zeizer T, Nitsure A. Performance comparison of different parallel lattice Boltzmann implementations on multi-core multi-socket systems. *Int JComputational Science and Engineering*. 2008;4:3-11.
- [37] Kruis J. Domain Decomposition Methods on Parallel Computers. In: Mota Soares CA, editor. *Progress in Engineering Computational Technology*. Stirlingshire UK: Saxe-Coburg Publications; 2004.
- [38] van Mier JGM, Shi C. Stability issues in uniaxial tensile tests on brittle disordered materials. *International Journal of Solids and Structures*. 2002;39(13):3359-72 DOI: [https://doi.org/10.1016/S0020-7683\(02\)00159-2](https://doi.org/10.1016/S0020-7683(02)00159-2).
- [39] FIB. CEB Bulletin 217 - CEB Bulletin 217. In: FIB-CEB, editor. 1993.
- [40] Nakamura H, Higai T. Compressive Fracture Energy and Fracture Zone Length for Concrete. In: ASCE, editor. *Modeling of Inelastic Behavior of RC Structures under Seismic Loads*. USA2001.

- [41] Krajcinovic D, Fonseka GU. The continuous damage theory of brittle materials. *Journal of Applied Mechanics*. 1981;48:809–24.
- [42] Kachanov M. *Introduction to continuum damage mechanics* 1986.
- [43] Bazant ZP. Nonlocal damage theory based on micromechanics of crack interaction. *Journal of Engineering Mechanics ASCE*. 1994;120:593–617.
- [44] Bazant ZP, Pijaudier-Cabot G. Measurement of characteristic length of nonlocal continuum. *J Eng Mech*. 1989(67):115-755.
- [45] Nakamura H, Nanri T, Miura T, Roy S. Experimental investigation of compressive strength and compressive fracture energy of longitudinally cracked concrete. *Cement and Concrete Composites*. 2018;93:1-18 DOI: <https://doi.org/10.1016/j.cemconcomp.2018.06.015>.
- [46] Jansen DC, Shah SP. Effect of Length on Compressive Strain Softening of Concrete. *Journal of Engineering Mechanics*. 1997;123(1):25-35 DOI: doi:10.1061/(ASCE)0733-9399(1997)123:1(25).
- [47] Hilsdorf HK, Brameshuber W. Code-type formulation of fracture mechanics concepts for concrete. *International Journal of Fracture*. 1991;51(1):61-72 DOI: 10.1007/bf00020853.
- [48] FIB. The fib Model Code 1999 for Concrete Structures, Model Code. International Federation for Structural Concrete. In: Sohn E, editor. Switzerland, Lausanne: FIB; 1999.
- [49] Hillerborg A. *Stability problems in fracture mechanics testing*: Elsevier Applied Science, 1989.
- [50] FIB. fib Bulletin No. 70 - Code-type models for structural behaviour of concrete. In: CEB-FIP, editor. Lausanne, Switzerland 2013. p. 196.
- [51] Pepe M, Grabois TM, Silva MA, Tavares LM, Filho RDT. Mechanical behaviour of coarse, lightweight, recycled and natural aggregates for concrete. *Proceedings of the Institution of Civil Engineers - Construction Materials*. 2020;173(2):70-8 DOI: 10.1680/jcoma.17.00081.
- [52] Pacheco JN, de Brito J, Chastre C, Evangelista L. Bond of recycled coarse aggregate concrete: Model uncertainty and reliability-based calibration of design equations. *Engineering Structures*. 2021;239:112290 DOI: <https://doi.org/10.1016/j.engstruct.2021.112290>.
- [53] Alfarah B, López-Almansa F, Oller S. New methodology for calculating damage variables evolution in Plastic Damage Model for RC structures. *Engineering Structures*. 2017;132:70-86 DOI: <https://doi.org/10.1016/j.engstruct.2016.11.022>.
- [54] Oliver J. A consistent characteristic length for smeared cracking models. *International Journal for Numerical Methods in Engineering*. 1989;28:461-74.
- [55] Mier J. *Concrete Fracture: A Multiscale Approach* 2012.
- [56] Geers MGD, Brekelmans WAM, de Borst R. *Viscous Regularization of Strain-Localisation for Damaging Materials*. Dordrecht: Springer Netherlands; 1994. p. 127-38.

- [57] Lopes B, Arruda MRT, Almeida-Fernandes L, Castro L, Silvestre N, Correia JR. Assessment of mesh dependency in the numerical simulation of compact tension tests for orthotropic materials. *Composites Part C: Open Access*. 2020;1:100006 DOI: <https://doi.org/10.1016/j.jcomc.2020.100006>.
- [58] Hassanzadeh M. Behaviour of fracture process zones in concrete influenced by simultaneously applied normal and shear displacements. Lund, Sweden.: Lund Institute of Technology, Ph.D Thesis, 1991.
- [59] Comi C. A non-local model with tension and compression damage mechanisms. *European Journal of Mechanics A/Solids*. 2001;20:1-22.
- [60] Comi C, Perego U. Fracture energy based bi-dissipative damage model for concrete. *International Journal of Solids and Structures*. 2001(10):227-42.
- [61] Mendes LAM. Refined Three-dimensional Seismic Analysis of Reinforced Concrete Structures [Ph.D. Thesis]. Lisbon: Instituto Superior Técnico, Ph.D. Thesis, 2011.
- [62] Winkler B. Traglastuntersuchungen von unbewehrten und bewehrten Betonstrukturen auf der Grundlage eines objektiven Werkstoffgesetzes für Beton. Austria: University of Innsbruck, Ph.D, 2001.
- [63] Yin Y, Qiao Y, Hu S. Four-point bending tests for the fracture properties of concrete. *Engineering Fracture Mechanics*. 2019;211:371-81 DOI: <https://doi.org/10.1016/j.engfracmech.2019.03.004>.
- [64] Desayi P. Fracture of concrete in compression. *Matériaux et Construction*. 1977;10(3):139-44 DOI: 10.1007/BF02474846.
- [65] Firmo JP, Arruda MRT, Correia JR. Numerical simulation of the fire behaviour of thermally insulated reinforced concrete beams strengthened with EBR-CFRP strips. *Composite Structures*. 2015;126(0):360-70 DOI: <http://dx.doi.org/10.1016/j.compstruct.2015.02.084>.
- [66] Firmo JP, Arruda MRT, Correia JR, Rosa IC. Three-dimensional finite element modelling of the fire behaviour of insulated RC beams strengthened with EBR and NSM CFRP strips. *Composite Structures*. 2018;183:124-36 DOI: <https://doi.org/10.1016/j.compstruct.2017.01.082>.
- [67] Firmo JP, Correia JR. Fire behaviour of thermally insulated RC beams strengthened with EBR-CFRP strips: Experimental study. *Composite Structures*. 2015;122(0):144-54 DOI: <http://dx.doi.org/10.1016/j.compstruct.2014.11.063>.